

Complex Faulting in the Quetta Syntaxis: fault source modeling of the October 28, 2008 earthquake sequence in Baluchistan, Pakistan, based on ALOS/PALSAR InSAR data



By: Muhammad Usman

Master's Degree Thesis

Space Geodesy Research Laboratory, Department of Earth and Planetary Sciences, School of Science,
Hokkaido University, Sapporo, Japan

Dedicated to my parents, teachers and friends
who are the source of continuous guidance,
inspiration and fun

Acknowledgements

I am very much thankful to Prof. Masato Furuya for his dynamic guidance and supervision. When I entered in Space Geodesy laboratory, my knowledge about InSAR processing and fault modeling was very basic and limited. Prof. Furuya guided from very beginning and always welcomed my fundamental questions. He provided an open ground to learn, think freely and perform different kind of trial and errors during InSAR processing and fault modeling. So, I analyzed the data as I wanted and made a lot of mistakes. He always welcomed my mistakes and corrected them.

Another best thing about our Space Geodesy lab is that everybody here is very much friendly and cooperative. I am thankful to all the teachers and lab mates for making my graduation time very memorable. I am especially thankful to Dr. Takatoshi Yasuda (currently a post doctorate fellow in our lab) and Mr. Shutaro Umemura (who graduated from our lab in March 2015) for their support and guidance during the process of this research.

PALSAR level 1.0 data in current research was provided by the PIXEL (PI Taku Ozawa). The ownership of PALSAR data belongs to Japan Aerospace Exploration Agency (JAXA) and the Ministry of Economy, Trade and Industry (METI/Japan).

Table of Contents

Title	Page #
Abstract	5
1. Background	6
2. Synthetic Aperture Radar	11
2.1 A comparison between ENVISAT/ASAR and ALOS/PALSAR	11
2.2 InSAR Processing and Results by using ALOS/PALSAR Data	12
3. Discussion and Conclusions	20
4. Trial and Error Procedure	22
5. References	24

Abstract

The Quetta Syntaxis in the western Baluchistan, Pakistan, is formed as a result of oroclinal bend of the western mountain belt and serves as a junction for different faults. As this area also lies close to the left lateral strike slip Chaman fault, which is supposed to be marking the boundary between Indian and Eurasian plate, the resulting seismological behavior of this regime becomes even more complex. In the region of Quetta Syntaxis, close to the fold and thrust belt of Suleiman and Kirthar ranges and on 28 October 2008, there stroke an earthquake of magnitude 6.4 (M_w) which was followed by a doublet on the very next day. In association with these major events, there have been six more shocks, one foreshock and five aftershocks that have moment magnitude greater than 4. On the basis of seismological, GPS and ENVISAT/ASAR data numerous researchers tried to explain the source of this sequence. Here ALOS/PALSAR InSAR data sets have been used from both ascending and descending orbits that allow us to more completely detect the deformation signals around the epicentral region. The results have indicated that the shock sequence can be explained with two right lateral and two left lateral strike slips that also include reverse slip. The right lateral faults have curved geometry. Moreover, the previous studies that have explained the aftershock crustal deformation with a different fault source; however in the present research it became clear that the same left lateral segment of the conjugate faulting is responsible for the aftershocks. The complex surface deformation signals even from the moderate-sized earthquake are thus confirmed. Intra-plate crustal bending and shortening seem to be often accommodated as conjugate faulting without any single preferred fault orientation. Two possible landslide areas have also been detected along with the crustal deformation pattern.

1. Background

Pakistan lies at the collision zone between the Indian and Eurasian Plate (Fig. 1). Resulting from this collision, the northern, western and southern sides of Pakistan are populated with many faults that remain active and also cause some major earthquakes from time to time posing a lot of damage to lives and infrastructures. Seismological hazardous zones of Pakistan with the known faults are shown in Fig. 2. For a developing country like Pakistan such disasters create a havoc as majority of the population lives in the mud build houses or having structures that are not resistant enough to the major or even the moderate earthquakes. It is estimated that around 2/3rd part of Pakistan is covered with faults. In the present research, the study area is located on the western side of Pakistan. This area are very complex tectonic structures as the Indian plate is moving northward at a rate of ~40 mm/yr, and its western margin is colliding with the Eurasian plate in Afghanistan and Pakistan. The relative plate motion would be partially accommodated by the prominent ~800 km-long Chaman fault. It is assumed that the Chaman fault is situated at the boundary between the two plates. The location of left lateral Chaman fault close to the Quetta Syntaxis, where many thrust faults are assumed to be joining (Fig. 3), results in a regime with a complex seismological behavior. The structural units have no ill defined pattern of strain orientation and result in the complex geological features (Figs. 3 and 4). While the Kirthar Range to the southwest is verging eastward, the Sulaiman Lobe is verging southward and the Sulaiman Range is eastward-verging (Figs.3 and 4). The sandbox modeling suggested that the relatively rigid Katawaz block to the north of Sulaiman Lobe played an important role to partition the strain (Haq and Davis 1997). By the inversion of strain field Bernard et al (2000) reached the similar conclusion. The Quetta Syntaxis is presumably formed as a result of oroclinal bend of these mountain belts (Fig. 1), and is expected to serve as a junction for thrust faults.

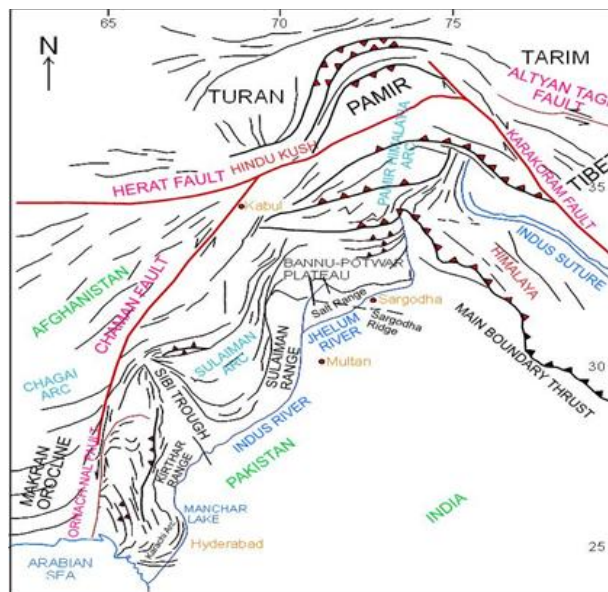


Figure 1. Regional tectonics of Pakistan (Kazmi and Jan, 1997)

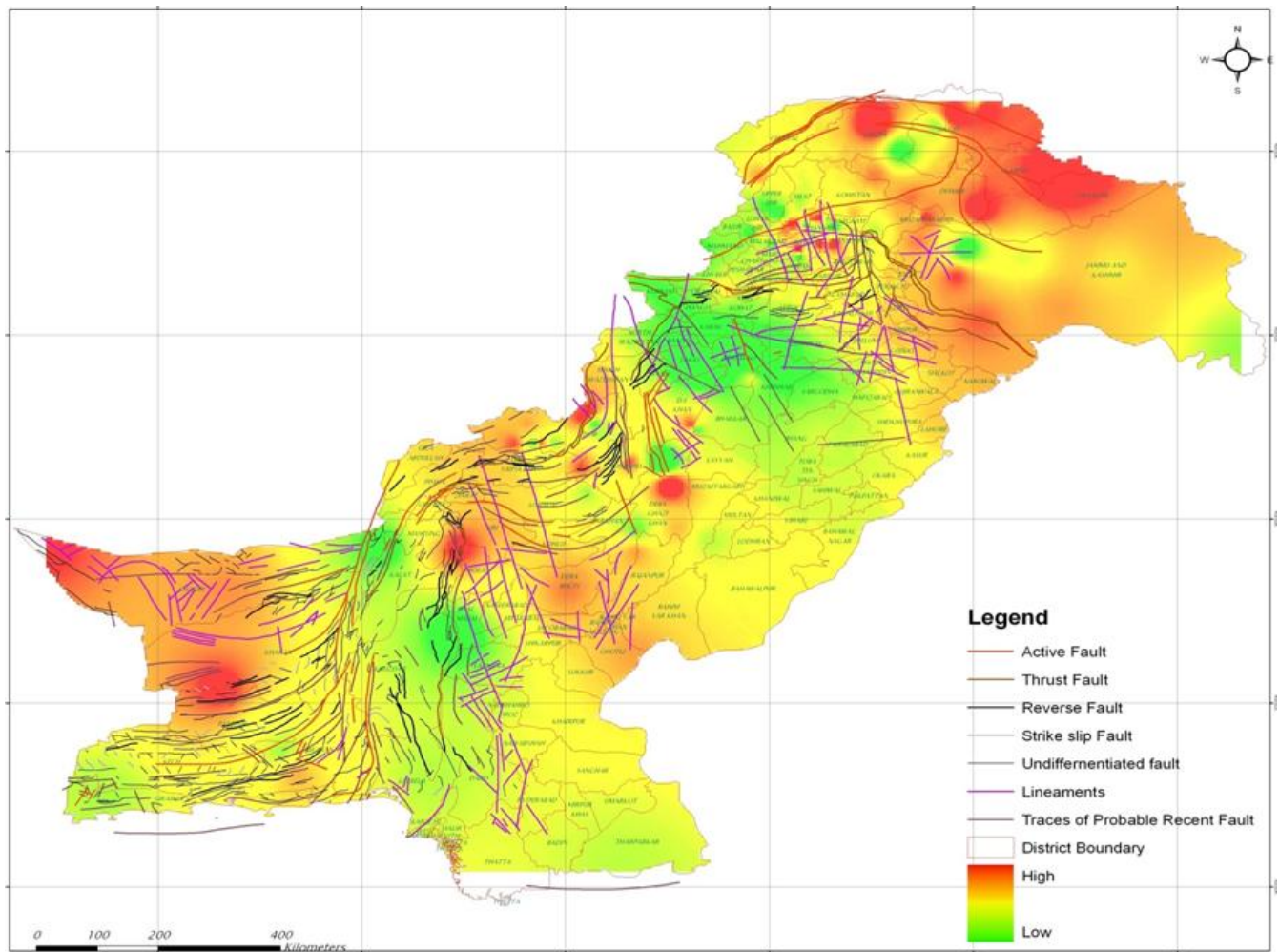


Figure 2. Seismologically hazardous areas and detailed tectonics of Pakistan (image courtesy of seismic section Pakistan Meteorological Department)

Close to the region of Quetta Syaxis, there stroke an earthquake of magnitude 6.4 (Mw) On October 28, 2008 (Fig. 2). It was followed by a doublet on the very next day (Table 1). The examination of the Focal mechanism solutions for earthquakes showed that strike slip mechanism, which was unexpected in light of the dominance of nearby thrust faults (Yadav *et al.*, 2012). 53 minutes before of the main shock and on October 28, 2008 there was one foreshock of magnitude 5.3. Four days after the main shock, there stroke the aftershock of magnitude 4.9 (Mw). Seventeen days after the main shock stroke another earthquake with magnitude 4.8. On December 12, 2008 there stroke three earthquakes on the same day that were having magnitudes 5.2, 5.3 and 5.7 respectively.

On the basis of GPS data study, Khan *et al.*, (2008) suggested NW-SE oriented right lateral slip associated with shock sequence of October 28, 2008. Based on seismological data study, Lisa and Jan (2010) proposed either one NNW trending Urghargai Fault or two parallel faults can be the source of the earthquake doublet. Based on the spatial distribution of aftershocks and the focal mechanisms, Yadav *et al* (2012) attributed the

earthquake sequence to the activation of the right-lateral strike slip Urghargai Fault (Fig. 2) that had been proposed by Kazmi (1979).

The co-seismic deformation signals derived from interferometric synthetic aperture radar (InSAR) technique have wide spatial coverage so they are more effective to identify the source of the earthquake (Massonnet et al., 1993; Amarjarga et al., 2013). Based on the C-band (5.6 cm wavelength) ENVISAT Advanced Synthetic Aperture Radar (ASAR) images, Pezzo *et al.* (2014) and Pinel Puysségur *et al.* (2014) produced the co-seismic inteferograms and proposed a complex geometry of the fault sources.

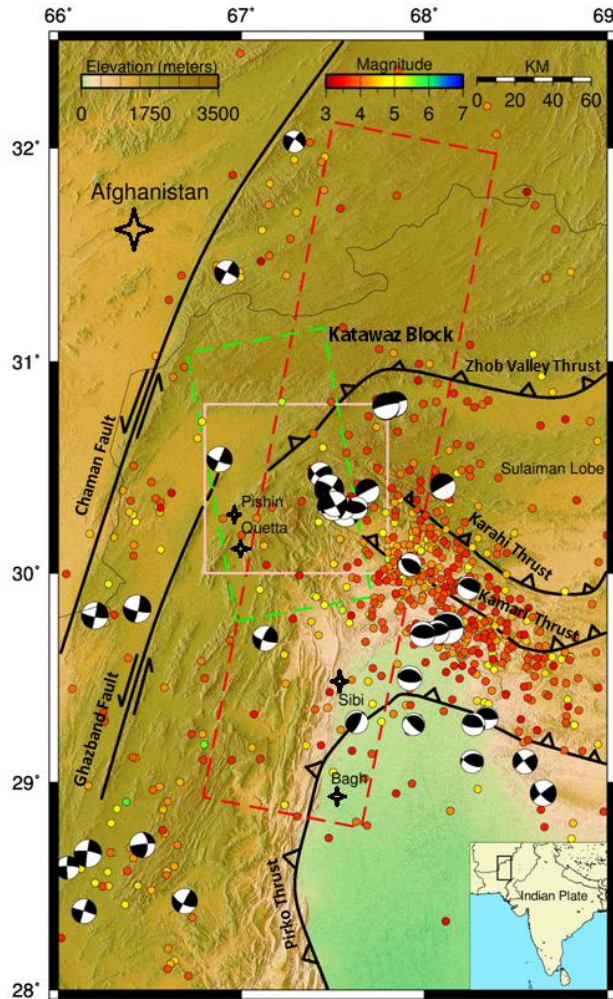


Figure 3. Regional tectonics of the study area. Faults are from Bannert et al., (1995). The International Seismological Center (ISC) earthquake catalog and The Global Centroid Moment Tensor (GCMT) data from 1976 to 2009 have been plotted. On top of the figure, the left scale is displaying the relative heights of the area in meters, the central color scale shows the magnitude of earthquakes ranging from 3 to 7 and right scale shows distance in kilometers (KM). The color dots show the location of corresponding magnitudes. The beach balls show the behavior and location of earthquake sources. The range of magnitude is from 5 to 6.4 (Mw) and size of beach balls is directly proportional to the corresponding magnitudes. The two dashed rectangles show the observations of satellite along ascending path 543 (green) and along descending path 193 swath 2 (red). The area inside the pink rectangle has been shown in Fig. 4 and Fig. 16.

ENVISAT/ASAR has lacked signals on the epicenter due to the low coherence and noises in the data. So, it has led to the different fault models despite the fact that they have used the same satellite data.

I have used Advanced Land Observing Satellite's Phased Array-type L-band (23.6 cm wavelength) Synthetic Aperture Radar (ALOS/PALSAR) data and have derived the co-seismic and aftershock deformation signals that provide us the maximum information on the epicenter. Although Pinel-Puysségur *et al* (2014) showed one InSAR image based on the ALOS/PALSAR, the InSAR data covered only a part of the entire deforming areas because the analyzed track was shifted to the east. The modeling done by using ALOS/PLASR data will provide us an insight to understand the local complexity and its implications for the regional strain partitioning and the style of intraplate deformation.

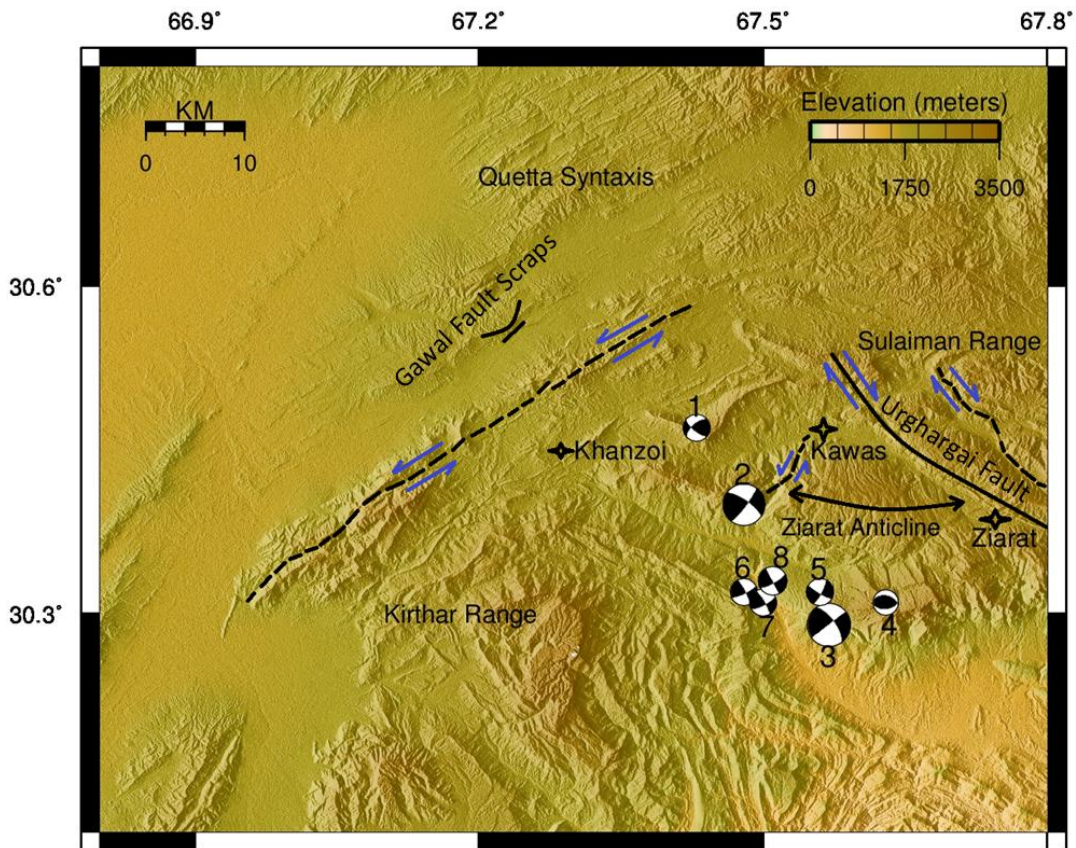


Figure 4. Detailed tectonics of the study area. The black lines are the previous mapped faults (Kazmi, 1979; Nakata et al., 1991) the dashed lines are the fault traces marked on the basis of morphology (Pinel-Puysségur *et al.* 2014). The FMS are plotted on the basis of GCMT data. The general trend of the faults, parallel to the right lateral Urgharghai fault, is right lateral and parallel to the Chaman fault is left lateral. The FMS 2 and 3 show the location and behavior of earthquake doublet that occurred on the dates 28, 29 October 2008, respectively. The remaining focal mechanism solutions show the location of associated earthquakes, having magnitude greater than 4 (Mw). The source parameters of these shocks are given in the Table 1.

Table 1. International Seismological Center (ISC) event data that have magnitude (Mw) greater than 4 and which is related to the shock sequence of October 28, 2008 in Baluchistan, Pakistan. The time indicated is universal time (UTC). Their corresponding FMS are shown in Fig. 4.

Earthquake #	Time (UTC) (HH:MM:SS)	Date (YY-MM-DD)	Lat	Lon	Mag. (Mw)
1	22:33:10	2008-10-28	30.5163	67.5639	5.3
2	23:09:58	2008-10-28	30.5928	67.3746	6.4
3	11:32:41	2008-10-29	30.4973	67.5633	6.4
4	16:08:15	2008-11-03	30.4102	67.7571	4.9
5	15:21:10	2008-11-15	20.4918	67.5710	4.8
6	02:46:31	2008-12-09	30.3569	67.5130	5.2
7	05:53:41	2008-12-09	30.3563	67.5179	5.3
8	22:52:37	2008-12-09	30.3912	67.4238	5.7

Table 2. ALOS/PALSAR data used in this research (Dates are formatted as YYMMDD) The A and D in the orbit stand for ascending and descending, respectively.

Orbit	Path	Frame/Swath	Mode	Dates	Perpendicular Baseline (m)
A	543	590-600	FBS	20071227-20100216	56
A	543	590-600	FBS	20081113-20090213	629
D	193	2	ScanSAR	20070211-20091216	-785

2. Synthetic Aperture Radar

The microwave imaging system Synthetic Aperture Radar (SAR) has cloud-penetrating capabilities. As it is active system, so it operates equally in the days and nights. One can measure the accurate travel path of the radiations as Interferometric SAR or InSAR is coherent. By using the Measurements of travel path variations as a function of time one can generate Digital Elevation Map (DEM) and can measure surface deformations of the terrain to the accuracy of centimeters.

2.1 A comparison between ENVISAT/ASAR and ALOS/PALSAR

ENVISAT ASAR: After two European Remote Sensing (ERS) satellites followed the ENVISAT. It is more advanced it is advanced and has: radar altimeter and temperature-measuring radiometer instruments extend ERS data sets. It is a medium-resolution spectrometer sensitive to both land features and ocean color. It has also instruments to collect data of trace gases. Its operation was needed in 2012. ENVISAT carries a sensor Advanced Synthetic Aperture Radar (ASAR) that has wavelength of 5.6 centimeters.

ALOS/PALSAR: Following the Japanese Earth Resource Satellite-1 (JERS-1) the Advanced Land Observing Satellite (ALOS) was launched from Tanegashima Island, Japan on 24 January 2006. The ALOS has three sensors: i) the Panchromatic Remote-sensing Instrument for Stereo Mapping (PRISM) for digital elevation mapping ii) the Advanced Visible and Near Infrared Radiometer type 2 (AVNIR-2) for precise land coverage observation iii) the Phased Array type L-band Synthetic Aperture Radar (PALSAR) for day-and-night and all-weather land observation. The Phased Array type L-band Synthetic Aperture Radar (PALSAR) has wavelength of 23.6 cm. PALSAR works with Fine Beam mode but it also has a ScanSAR that can cover the width of 250 to 350km but at the expense of spatial resolution.

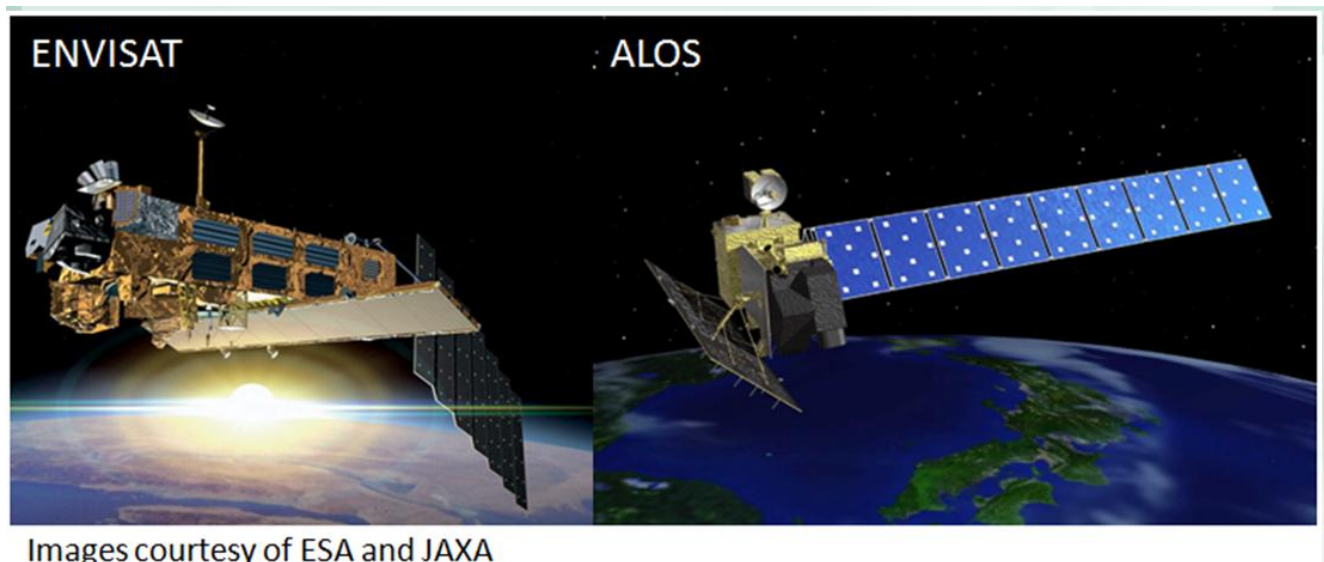


Figure 5. ENVISAT and ALOS

2.2 InSAR Processing and Results by using ALOS/PALSAR Data

First, I have processed the data along the ascending path 542 of the ALOS/PALSAR (Fig. 6). But it was not providing the enough information of the epicentral area so I moved to the next path 543. This path has provided a very good observation on the epicentral region (Fig. 7). Along the path 543, The Fine Beam Single Polarization (FBS) data sets are available and have been used to generate two interferograms: the first one covering the seismic sequence and the second covering the shocks on December 09, 2008 (Table 2). The microwave's incidence angle in the image center of the ascending FBS mode is 38.7 degrees. As PALSAR produces limited fine beam data along the descending path so the swath-2 image of the ScanSAR mode data along the path 193 was used and it was completely covering the epicenter region. The radar incidence angle at the center of the swath-2 image is 29.4 degrees.

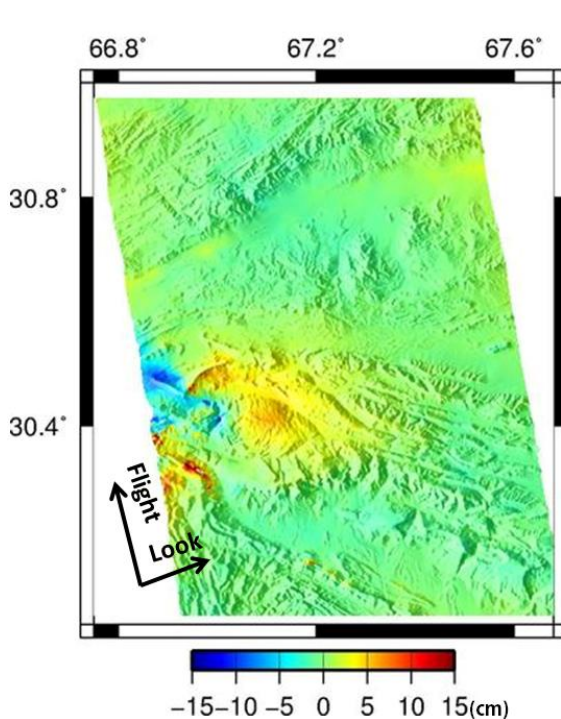


Figure 6. Image along ascending path 542 of ALOS/PALSAR: (Master: Jan22, 2007-Slave: Dec12, 2008)

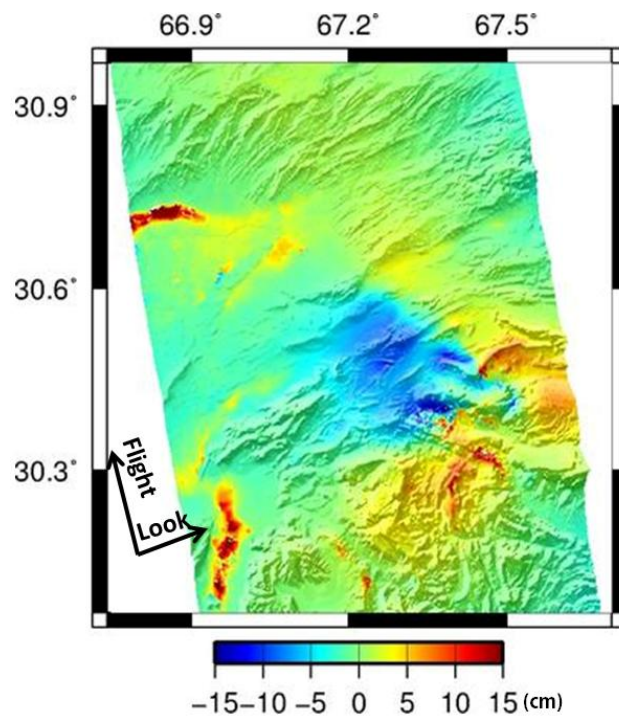


Figure 7. Image along ascending path 542 of ALOS/PALSAR: (Master: Feb08, 2007-Slave: Feb13, 2009)

To process the InSAR data the techniques are same as used in the previous researches (Kobayashi *et al.*, 2009; Furuya *et al.*, 2010; Furuya and Yasuda, 2011, Abe *et al.*, 2013). The data was processed by using the commercial software package Gamma Remote Sensing. In this research, the level 1.0 PALSAR image has been used. By using the Digital Elevation Model (DEM) from Shuttle Radar Topography Mission (SRTM) (Jarvis *et al.*, 2008) the topographic fringe was removed. To remove the orbital fringes, the high precision orbital data provided from Japan Aerospace exploration Agency (JAXA) was used. The Figs. 7, 8a, and 5a show the observed ground displacement for the ascending and Fig. 4a show the observed crustal deformation

for the descending path. The scale has positive values having red color and negative value having the blue color in the Figs. 6, 7 8a, 9a and 10a indicate the range change along the radar line of sight that is away from and toward the satellite, respectively. The linear combination of 3D displacement results in the range change and it is equal to $+0.62U_e+0.11U_n-0.78U_z$ for the ascending and $-0.48U_e+0.09U_n-0.87U_z$ for the swath-2 of the descending image, respectively; Here U_e , U_n , and U_z are taken as the positive eastward, northward, and upward components, respectively. For the main shock, the amplitude is around 15 cm for the ascending (Figs. 6,7,8a) and 17 cm for descending images (Fig. 9a), respectively; I have observed nearly the same amplitude in both positive and negative range changes. In both Figs. 8a and 9a, NW-SE and NE-SW striking boundaries can be identified across which the signs have changed. The phase-boundaries are attributed to the top edge of two fault segments, RLF1 and LLF1.

Close to the central part of RLF1, breaks in the deformation pattern has been found that suggest a bend in the fault surface at this area (Figs. 8a and 9a). For both ascending and descending InSAR observations, the data indicates that this part has moved towards the satellite (Figs. 8a, 9a). The study of the fault mechanism solutions (Fig. 2) indicates that the inclusion of a reverse component in most of the shocks and the fault mechanism for the no. 4 exhibits an almost pure reverse faulting. These observations strengthen the possibility of uplift in this area.

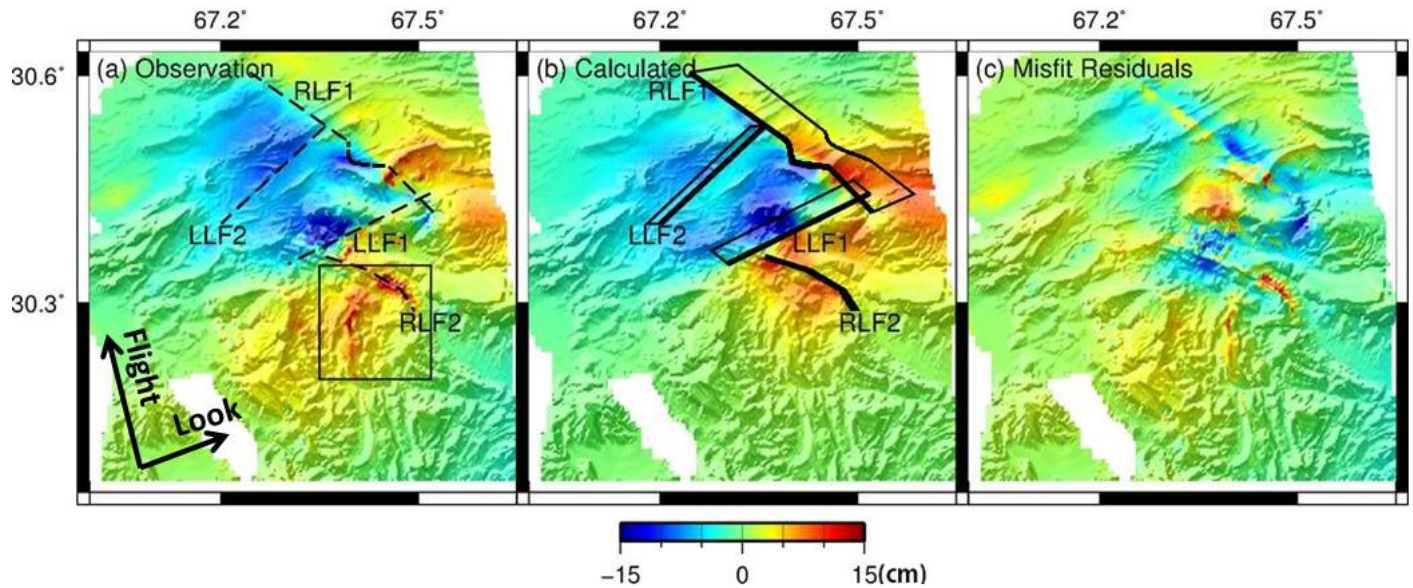


Figure 8. (a) Observed InSAR data acquired along the ascending track 543. (b) Computed InSAR data based on the fault model shown in Fig. 10. Two Right Laterals Faults (RLF1, RLF2) trending is the NW-SE direction and two Left Lateral Faults (LLF1, LLF2) having strike direction NE-SW. The thicker line shows the top edge of the faults. (c) Misfit residuals between the observed and calculated signals. High amplitude signal area enclosed in the rectangle has been shown in the Fig. 11a. The color scale with positive and negative values shows the range changes along the radar line-of-sight, indicating the surface movement away and towards the satellite, respectively.

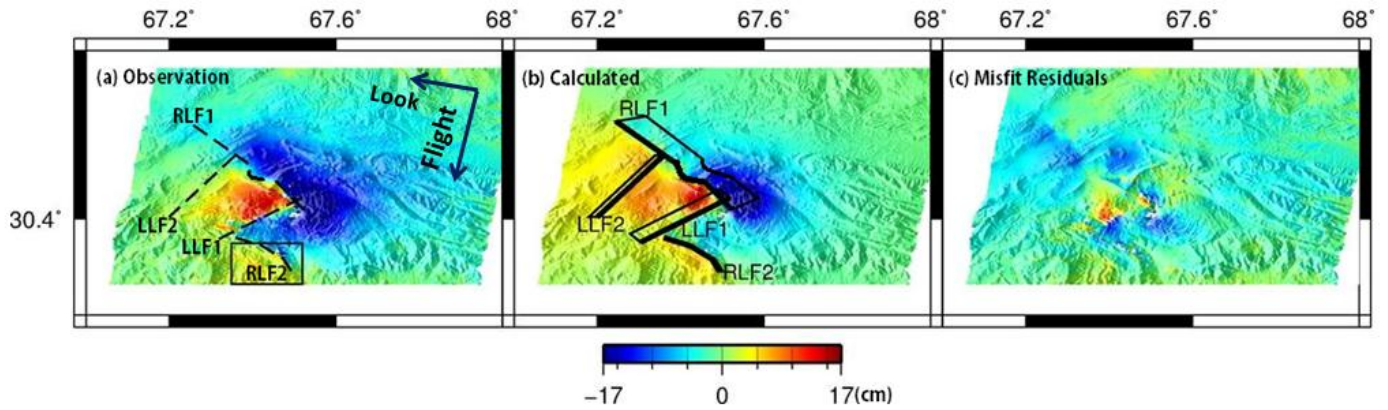


Figure 9. (a) Observation along descending path, covering the seismic sequence (b) The calculated model whose slip distributions for each segment is are shown in Fig. 10. The same fault geometry of four faults, which was used, is the ascending InSAR data i.e. RLF1, RLF2, LLF1 and LLF2, is shown here (c) Residual between observed and calculated data. High amplitude signal area enclosed in the rectangle has been shown in the Fig. 7a. The color scale with positive and negative values shows the range changes along the radar line-of-sight, indicating the surface movement away and towards the satellite, respectively.

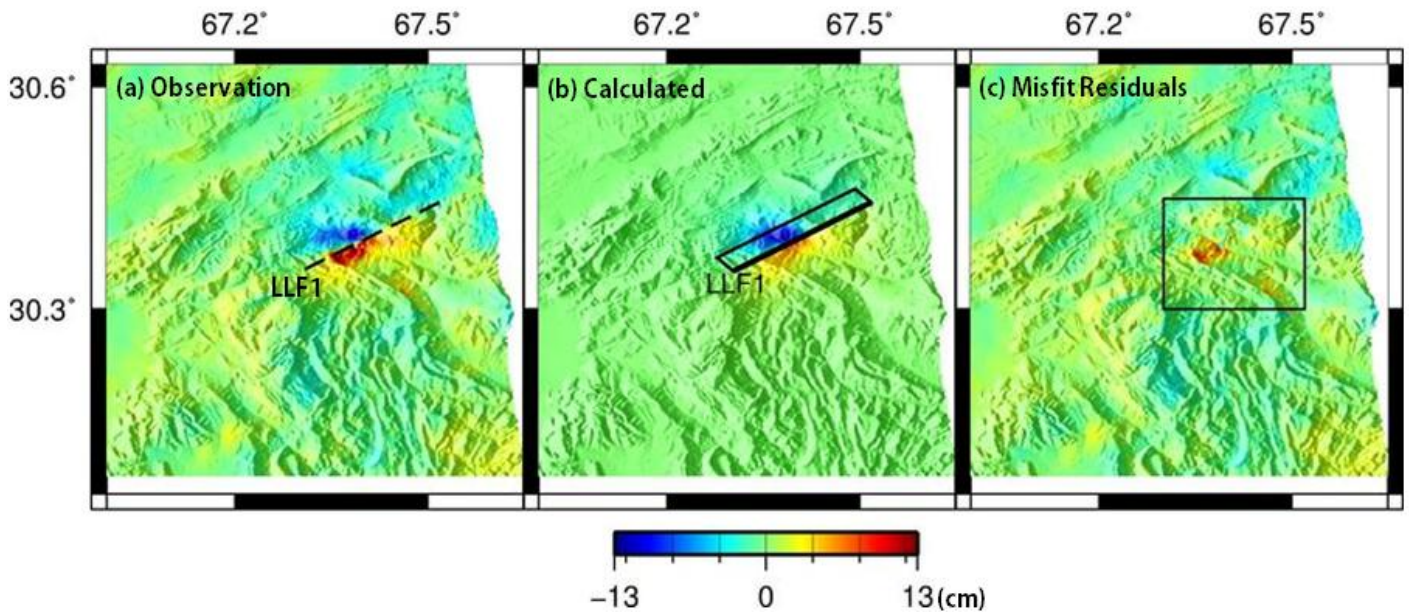


Figure 10. (a) Observation along the ascending path, covering the aftershocks of December 09, 2008 (b) Modeled signals: the same fault LLF1 of conjugate faulting, that was used to explain the deformation of the seismic sequence, has been used here. (c) Misfit residuals between the observed and modeled signals. The area enclosed in the black lines is shown in Fig. 12. The color scale with positive and negative values shows the range changes along the radar line-of-sight, indicating the surface movement away and towards the satellite, respectively.

There is also two shorter phase jumps: one strikes NE-SW it is designated as LLF2 (Figs. 8a, 9a) and second strikes NW-SE and it named as RLF2 (Figs. 8a, 9a). The amount of crustal deformation detected for the

aftershock is 13 cm for both positive and negative sense (Fig. 10a). Comparing the location of the phase boundary in Fig. 5a, it turns out that the phase-step location exactly matches the location for the LLF1 in Figs. 8a and 9a. The survey done in the earthquake areas has not indicated any clear co-seismic surface rupture (Khan *et al.* 2008). Thus the phase boundaries noted above have no corresponding surface faults. But there were some places where the cracks on the ground have been found (Zahid *et al.*, 2009). In Figs. 8a and 9a, there are no clear corresponding signals.

If the data covering the seismic sequence is observed then I could also identify positive range changes of around 14 cm in the NW and SW side of the interferogram that are outside the epicentral areas (Fig. 7). These study of these areas showed that the signals are coming from the populated areas, Haramzoi and Killihajezai in the Northwestern and Quetta in the Southwestern. It has led to conclude that these are signals due to subsidence as in these areas water extraction from underground is very common and can result in the downward movement of the earth. These areas containing the unwanted signals are masked for the fault source modeling.

Two high amplitude signals of around 17 cm have been observed that were localized in two regions. For the ascending data they were indicating a movement away from the satellite (Figs. 8a, 11a). On the other hand one area shows movement towards the satellite and second shows a movement away from the satellite for the descending data (Figs. 9a, 12a). These signals remain quite prominent in the residue (Figs. 8c, 9c) and the closer examination of topography (Figs. 11b, 12b) indicates that the high amplitude signal areas are located on the north-eastern and eastward dipping flank of the mountains. The study area seems very sensitive even to the earthquakes having moment magnitude around 5. As in the aftershock interferogram (Fig. 10a), I also notice a movement away from satellite having amplitude of around 8 cm has also been observed. Here also the signals are quite noticeable in the residue (Figs. 10c, 13a). It has led to conclude that these localized deformations would indicate the co-seismic landslides as they are coming from steeply dipping areas (Fig. 13b). As there are two possible reasons: i) the spatial scale is more localized than that due to the fault-related deformations ii) these cannot be due to errors in DEM as the perpendicular baselines (Table 2) is considerably small.

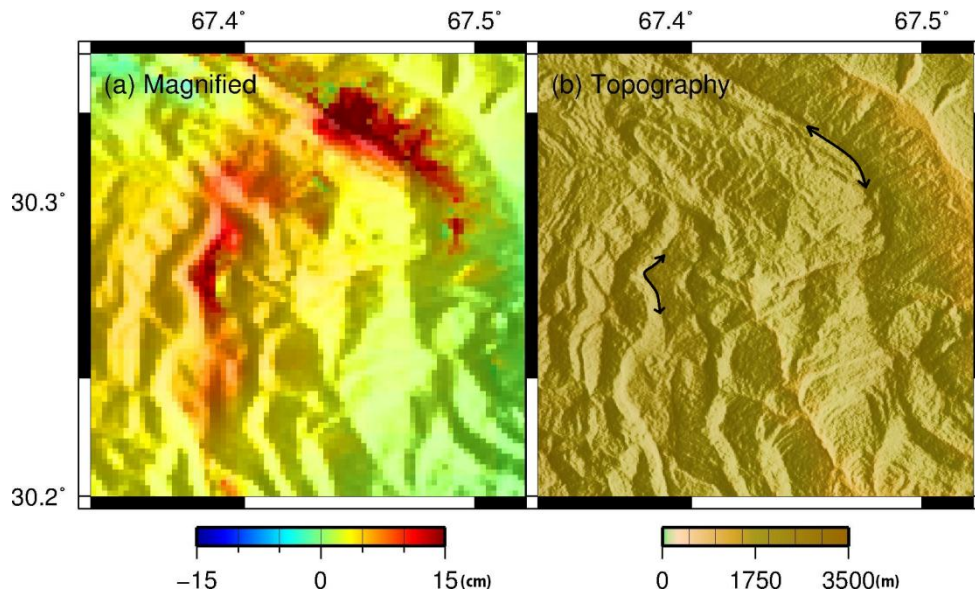


Figure 11. (a) Magnified view of the high signal areas located on the epicenter, along the ascending path, covering the seismic sequence (b) Topographic view to investigate the high signal areas.

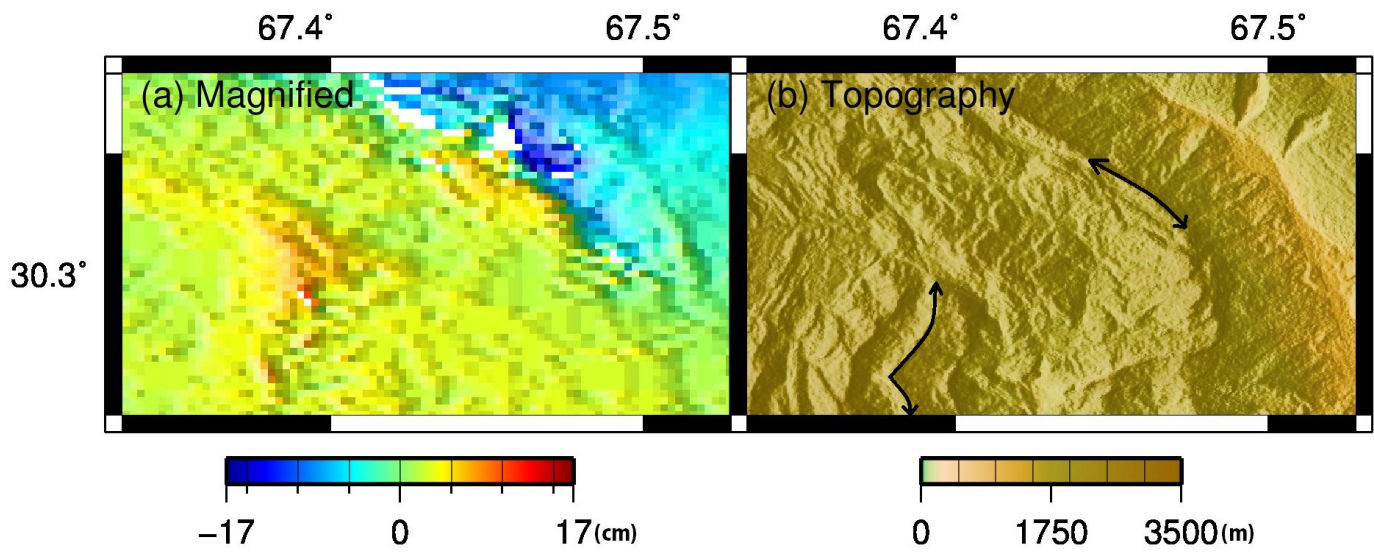


Figure 12. (a) Magnified view of the high signal areas located on the epicenter, along the descending path, covering the seismic sequence (b) Topographic view to investigate the high signal areas

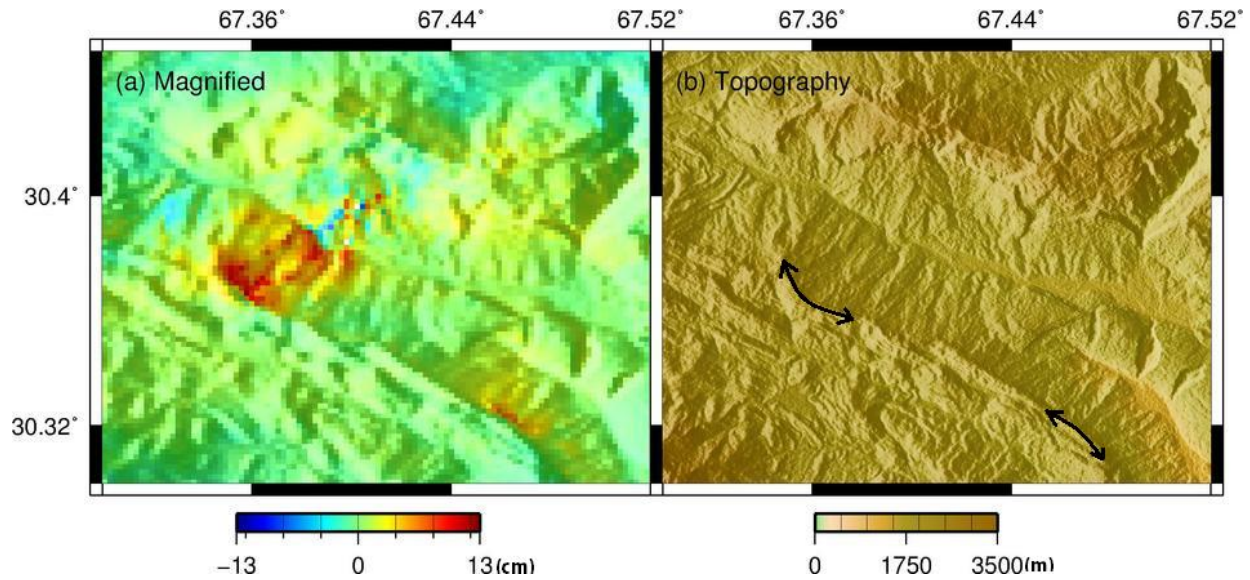


Figure 13. (a) Magnified view of the misfit residuals related to the December 09, 2008 aftershocks modeling (b) Topographic view

3. Fault Modeling Methodology and Results

Analytical solutions for the dislocations in an elastic half space are very useful to interpret the co-seismic deformation signals. Okada (1992) solutions are extensively used. However, as the Okada (1992)'s solutions, use rectangular dislocation element to express the displacement. Thus mechanically incompatible gaps or overlaps or both are generated in case of the actual dislocation sources have non-planar geometries (Maerten et al., 2005; Furuya and Yasuda, 2011; Abe et al., 2013). So Meade's (2007) analytical solutions were used here; as it uses a triangular dislocation element to estimate the fault slip from the observed ground displacements.

The crustal deformation pattern was carefully examined. The places where there was very strong possibility of a fault surface, over there, for each fault segment the 3D coordinates for several selected control points were picked up. To generate the fault surface, these points are interpolated with spline. To avoid unnecessary complications; mesh size for each triangulation dislocation was kept 2.5 kilometers and bottom and the top of the fault were kept parallel to each other. By the mesh generating software Gmsh (Geuzaine and Remacle, 2009) the 3D mesh coordinates for each node were generated automatically. Consequently, for each triangular slip patch the dislocation Green's Function was calculated. Then, slip distributions are inverted as a linear least-squares problem (e.g., Jónsson *et al.*, 2002; Simons *et al.*, 2002; Wright *et al.*, 2003). To reduce the data size, quad-tree decomposition was used (e.g., Jónsson *et al.*, 2002; Lohman and Simons, 2005). Both smoothness constraint on the slip distributions with scale-dependent umbrella operator (Maerten *et al.*, 2005) and a non-negativity constraint on the signs of the fault slip directions were also applied (Furuya and Yasuda, 2011; Abe *et al.*, 2013).

The focal mechanism solutions (Fig. 4) study shows that it is reasonable to expect that strike slip faulting is mainly responsible for generating the co-seismic ground displacements along with the inclusion of some reverse slip faulting (Table 1). The breaks in the deformation pattern suggest NW-SE trending right lateral fault RLF1 and NE-SW trending left lateral fault LLF1, forming a conjugate geometry (Figs. 8b and 9b). Along with these two major segments, RLF1 and LLF1, phase changes for two more segments were found. By observing the phase change striking in NW-SE direction in Fig. 4a, the segment is designated as RLF2. This is because the right lateral strike slip is mechanically feasible and consistent with the observed signs of phase changes. There is also a strong indication of another fault in the west of RLF1 in Fig 4a and it is named as LLF2. The location of this fault is consistent with the F¹2 by Pinel-Puysegur *et al.* (2014) and the 4th segment by Pezzo *et al.* (2014). After identifying the four faults, the optimum geometry was obtained after a lot of trial and errors (Figs. 8, 9 and 14). The detail of trial and error procedure is given in the section 5.

When the aftershock crustal deformation was studied (Fig. 10a), a clear phase discontinuity can be observed that trends NE-SW. When this location is compared with the interferogram covering the seismic sequence, the location of the top edge is exactly the same as that of LLF1 as noted above. So it has led to conclude that the same fault is also responsible for the shocks of December 09, 2008. The modeling done by using the same fault LLF1 has produced residuals in the accepted range (Fig. 10c) with logical slip distributions (Fig. 15). It means that same fault LLF1 has contributed in seismicity of seismic sequence but along with the aftershocks.

Table 3. Some fundamental parameters of proposed faults

Fault Name	Dip	Cal. Mag. (Mw)	Status
RLF1	81 ⁰	6.5	Covering Shock Sequence
RLF2	90 ⁰	6.2	Covering Shock Sequence
LLF1	84 ⁰	6.3	Covering Shock Sequence
LLF2	85 ⁰	5.9	Covering Shock Sequence
LLF1	84 ⁰	5.7	Covering the Aftershocks

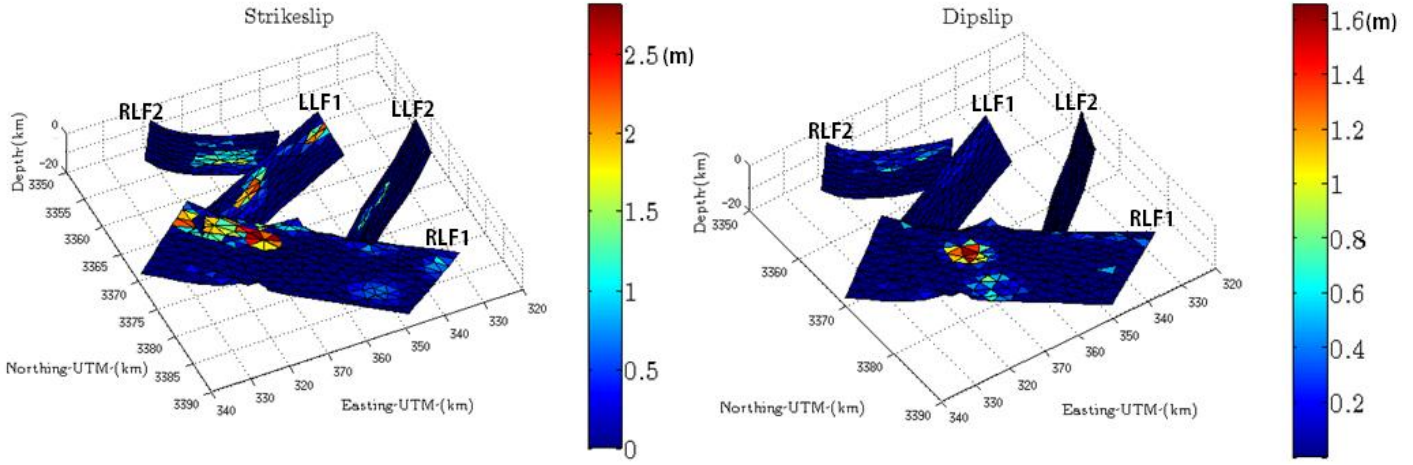


Figure 14. Slip distribution for the seismic sequence. The top of the faults is 300 meters below the crust surface. The calculated magnitude (M_w) for RLF1, RLF2, LLF1 and LLF2 is 6.5, 6.2, 6.3 and 5.9 respectively.

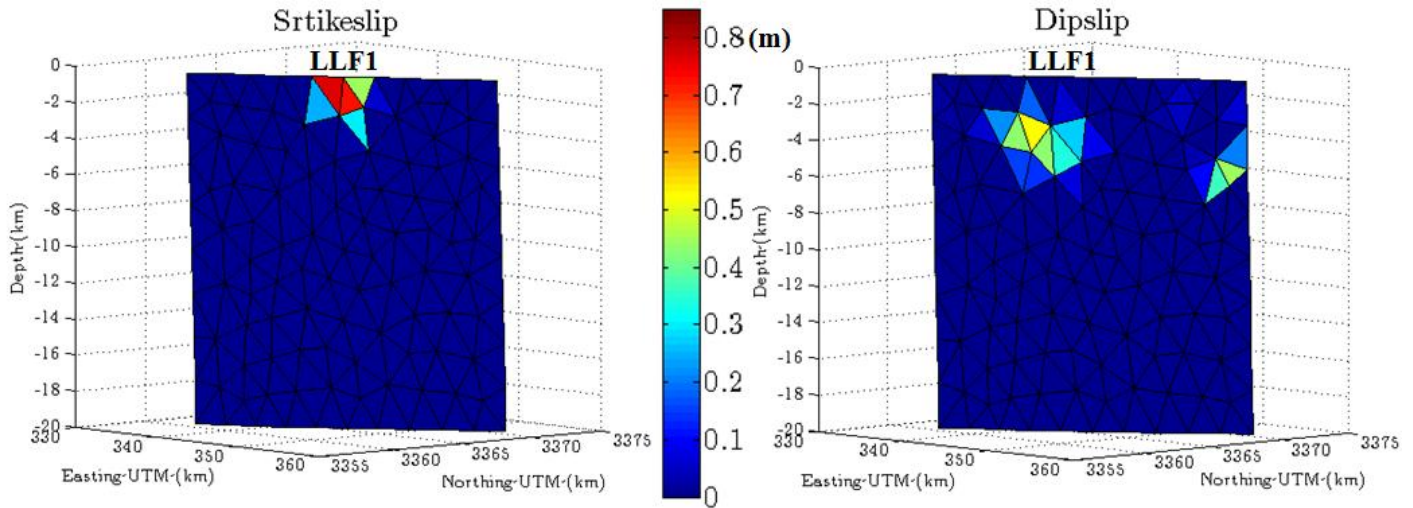


Figure 15. Slip distributions for the aftershocks of December 09, 2008. The calculated magnitude is 5.7 (M_w). The modeling has been done by using the same fault LLF1 of the conjugate faulting

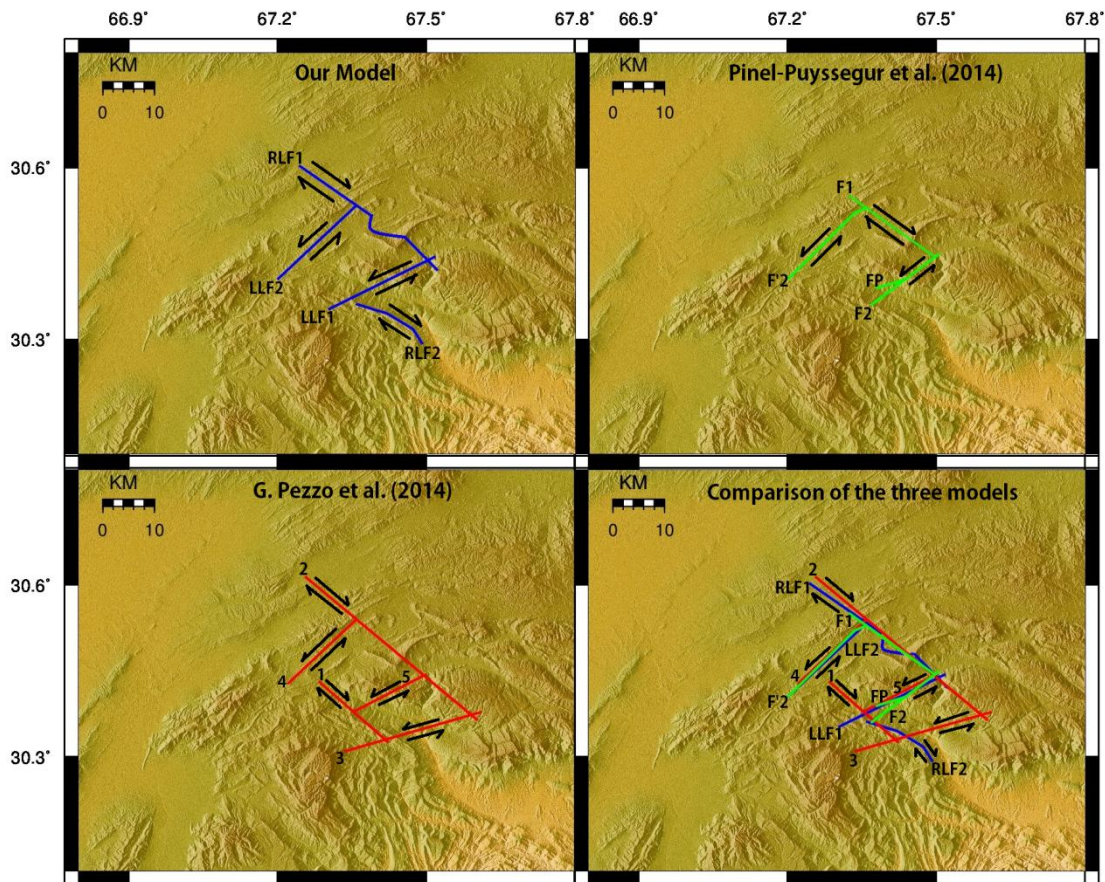


Figure 16. (Upper left) Our model; the location of top edges for each fault segment are shown with blue lines. (Upper right) The model by Pinel-Puysegur et al (2014) shown with green lines. (LoIr left) G. Pezzo et al., (2014) proposed model, displayed in red lines. (LoIr Right) Comparison between previous and present models.

3. Discussion and Conclusions

The moderate and major inland earthquakes pose a strong threat to the human life and infrastructure but at the same time their proper investigation gives us an insight to understand the regional strain partitioning and the style of intraplate deformation. SAR is an emerging tool and is providing us useful information on the epicenter, so I can propose a fault plane model that can explain the observed deformation with logical slip distributions. However, to produce a reliable model two aspects are the most important: maximum data coverage of the epicentral region and quality of the data. A data with high coherence and very less noises has great importance to explain the source of co-seismic deformation in the complex tectonic regimes like Quetta Syntaxis. This shock sequence has been studied by using the conventional methodology of seismology and also by the latest cutting edge technology of InSAR.

A single NW-SE trending fault was suggested by Yadav *et al.* (2012) and Khan *et al.* (2008), who analyzed seismological data and GPS data, respectively. Lisa and Jan (2010) suggest right lateral NNW-SSE oriented

faults along one or two parallel faults on basis of the epicenter distributions. By using the Interferometric Synthetic Aperture Radar from ENVISAT/ASAR C-band radar sensor, Pinel-Puysegur *et al.* (2014) suggested a four-fault model (three left laterals i.e. F2, F¹2 and FP and one right lateral F1)(Fig. 16). Meanwhile, Pezzo *et al.* (2014) proposed a five-fault model (three left laterals i.e. 3, 4 and 5 and two right laterals i.e. 1 and 2) (Fig. 16) by using the same ENVISAT/ASAR data. There are significant differences in these models which leave a lot of ambiguities related to the source orientations of the shock sequence of December 09, 2008. Probably these differences are attributed to the less coherence of the data on the epicenter which has led to lack of data. SAR data on the epicenter is very important for the inference of fault sources.

The comparison of the modeling geometry between previous and presents model are given in the Fig. 16. All three models agree at that there is a conjugate faulting. The segments F1, F2 in Pinel Puysegur *et al.* (2014), the faults 2, 3 in Pezzo *et al.* (2014) study and the RLF1 and LLF1 in our model are forming a conjugate geometry. The comparison of dip angles for the conjugate faults indicates that the right lateral segments i.e. fault 2 of Pezzo *et al.* (2014), F1 of Pinel *et al.* (2014) and RLF1 of our model have dips 75° , 73° and 81° respectively. On the other hand, the left lateral segments i.e. Fault 3 of Pezzo *et al.* (2014), F2 of Pinel *et al.* (2014) and LLF1 of our model have dips of 90° , 89° and 84° respectively.

Apart from the curved fault geometry for right lateral faults of our model (RLF1 and RLF2), there are also some other significant differences. In case of Pinel *et al.* (2014) study, ear the location of fault segment FP for the co-seismic interferogram, their InSAR data are noisy and subsequently the affected area was masked. The comparison of our model with Pinel *et al.* (2014) shows that segment F¹2 is very close in location and length to the LLF2 of our model. However, the conjugate faults of the Pinel *et al.* (2014) model are shorter in length have greater in the angle between them and their intersection point is shifted towards the western side in comparison to the conjugate geometry of our model. To explain the aftershock crustal deformation, Pinel *et al.* (2014) also suggested that it was caused by a different fault segment FP rather than the same segment of conjugate faulting (as LLF1 in our model). Also, the segment RLF2 is entirely missing in their study. On the other hand, Pezzo *et al.* (2014) have lacked many signals around the epicentral area. The fault 4 in Pezzo *et al.* (2014) looks quite close in its location and length to our fault LLF2 but the segment 3 is unnecessary. The segment 2 is very longer compared to the RLF1 of our model which is also curved at the center. The aftershock of December 09 was explained by segment 5 which looks very close in the location and length to the LLF1 of our model. However, if RLF2 is compared with the segment 1 than the segment 1 is crossing the segment 5 and penetrating into the block between segment 4 and 5. But no such breaks have been found in the ALOS/PALSAR data, in the area between LLF1 and LLF2 of our model. Rather, the ALOS/PALSAR data has led us to conclude that the segment RLF2 extends further towards SE direction.

If the slip distribution of our model is examined than the maximum slip is distributed on the conjugate faults. It gives an indication that these conjugate faults played a very important role during the seismic crisis of the 28 October 2008. Modeling also suggests that RLF2 has moment magnitude of 6.2. On the basis of tilt records, during the study of Iwate-Miyagi earthquake of 2008, Fukuyama (2015) categorized such

earthquakes with conjugate rupture planes into two groups: Namely, while the category-1 indicates the simultaneous rupture of both the main and conjugate rupture, the category-2 indicates the conjugate rupture after the main rupture. In Table 3, the moment magnitude computed from present fault model is indicated. Regardless of the fact that there were seismologically two earthquakes with Mw 6.4, it turns out that the moment magnitude of the three faults was greater than 6.2. Assuming that the rupture on the RLF1 was the first shock (FMS 2 in Fig. 4), it is likely that the category-1-type rupture on the LLF1 and RLF2 took place on the next day (FMS 3 in Fig. 4), because the combined magnitude seems to confirm to the seismological moment magnitude. Four days after the earthquake doublet, there was a shock having magnitude 4.9 (Mw) with nearly a pure reverse component (FMS 4 in Fig 4). Examination of the observed data (Fig. 8a and 9a) indicates that the area adjacent to the bending of RLF1 has moved towards the satellite i.e. uplifted. Our model also shows that maximum slip for the dip-slip (Fig. 14) is concentrated exactly below the curved area of RLF1. So probably the earthquake number 4 (Fig. 4) might be caused by RLF1. Also, as the position of LLF1 exactly matches with the location of breaks in the phase of the aftershock observed data Fig. 10a, so it is reasonable to believe that the shocks number 6, 7 and 8 in Fig. 4 are the result of seismological activity related to LLF1. However, it is difficult to determine the causative fault for shock number 1 and 5 (Fig. 4). Their relative positions give an indication that either LLF2 or RLF1 is the source fault for earthquake 1. For earthquake 5, either LLF1 or RLF1 is the responsible fault.

In the last decade complex surface deformations signals are being revealed from moderate-sized M6-class earthquakes. The conjugate geometry of the left lateral and right lateral fault was also inferred previously by Walker *et al.* (2013) who studied the earthquake sequence occurred in southeastern Iran on December 10, 2010 (Mw6.5) and January 27, 2011 (Mw6.2). Even in the thrust type earthquakes, such conjugate geometries in the intraplate earthquakes have also been reported. Both west-dipping and east-dipping thrust faults have been pointed out from PALSAR data, during the study of 2008 Iwate-Miyagi inland earthquake (Mw6.9), Japan (Takada *et al.*, 2009; Abe *et al.*, 2013). In these kinds of areas, a disturbed zone without any preferred fault orientation results due to Intraplate crustal bending and shortening. In the present research, the earthquake doublet has same focal mechanism solutions so there were a lot of ambiguities related to their fault planes, location and size of the source faults. If high coherence SAR data is available on the epicenter than it is very helpful to resolve such issues.

4. Trial and Error Procedure

Previous studies (Pinel *et al.*, 2014; Pezzo *et al.*, 2014) suggested straight fault geometry, and our data did not strongly indicate curved geometries, either. Thus, I have first tested different possibilities of depth and dips, by keeping the strike for all the faults straight. However, there always remained significant residuals, especially in the descending data, even for the best straight-fault model (Figs. 17, 18). To explain these unexplained signals, I have examined the data very carefully, and the descending observation Fig. 4a suggests a clear bend in the RLF1 around the central point. Also, the RLF2 exhibits a curved strike. The modeling done by following the curved geometry for right lateral faults (RLF1 and RLF2) has explained the observed deformation quite successfully (Figs. 8, 9, 14).

The study of fault mechanism solution (Fig. 4) suggests that the contribution of strike slip was dominant over the dip slip component for the co-seismic and for most of the aftershock crustal deformations. The maximum observed magnitudes are 6.4 and 6.4 (Mw) for the co-seismic and 5.7 (Mw) for the aftershocks (Table 1). So for the source modeling, the attempt was that to produce a model that exhibits nearly the same characteristics in terms of slip components and calculated magnitudes along with minimum possible residuals and logical slip distributions.

As it was established that LLF1 is contributing for both crustal deformations resulting from the co-seismic and aftershocks, I produced an optimum fault model (Figs. 10 and 15) by following the trial and error i.e. various possibilities related to the depth and dip of LLF1 were analyzed and the best result was selected. The LLF1, with the same geometry, was imported to the co-seismic model and here again a lot of trial and errors were performed by changing the depths and dips of RLF1, RLF2 and LLF2. The best model was selected (Figs. 3, 4 and 10) that has strike slip component dominant over the dip slip, maximum slip is distributed along conjugate faults (RLF1 and LLF1) and the calculated magnitude (Mw) is 6.3 for LLF1 and 6.5 for RLF1 which is very close to the observed moment magnitude.

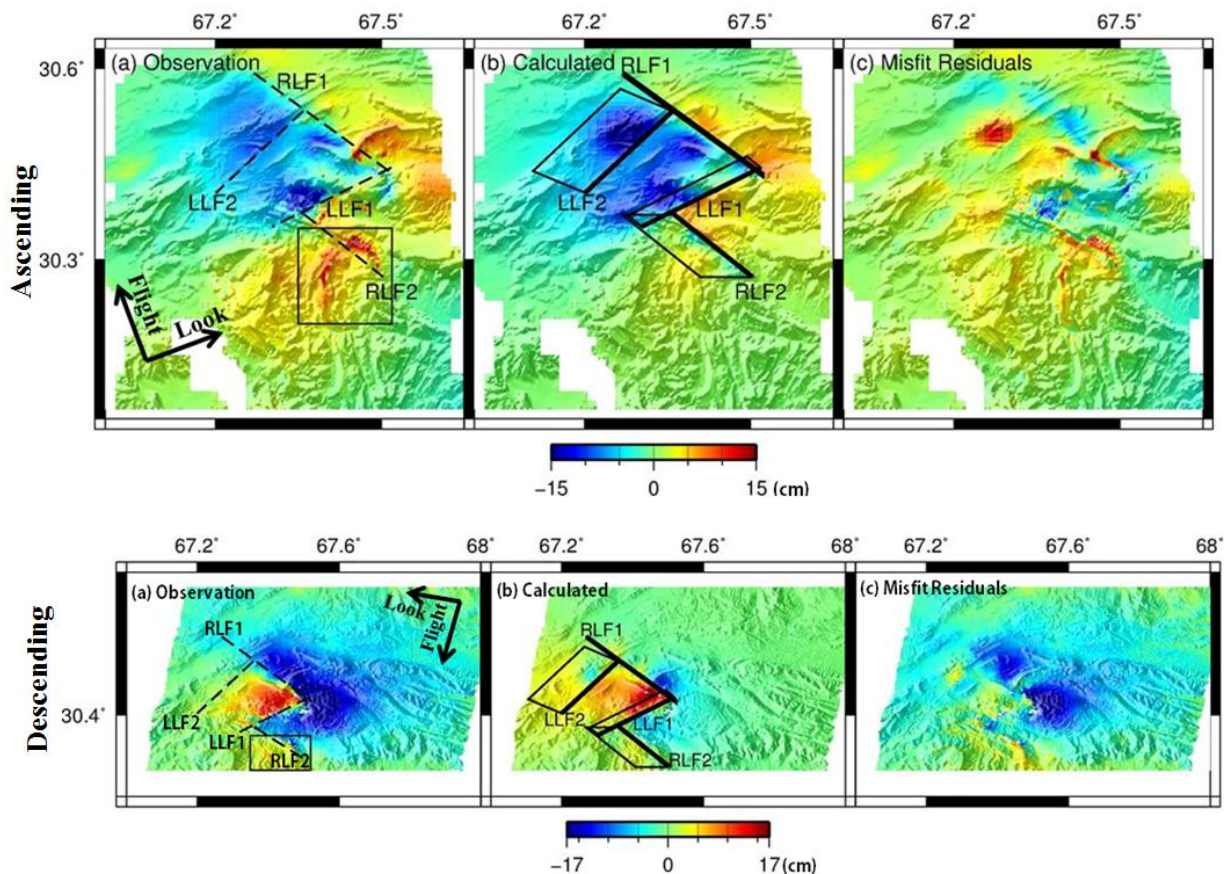


Figure 17. Modeling results following the straight fault geometry and the areas enclosed in rectangular boxes in the descending and ascending observation are shown in Figs. 6 and 7.

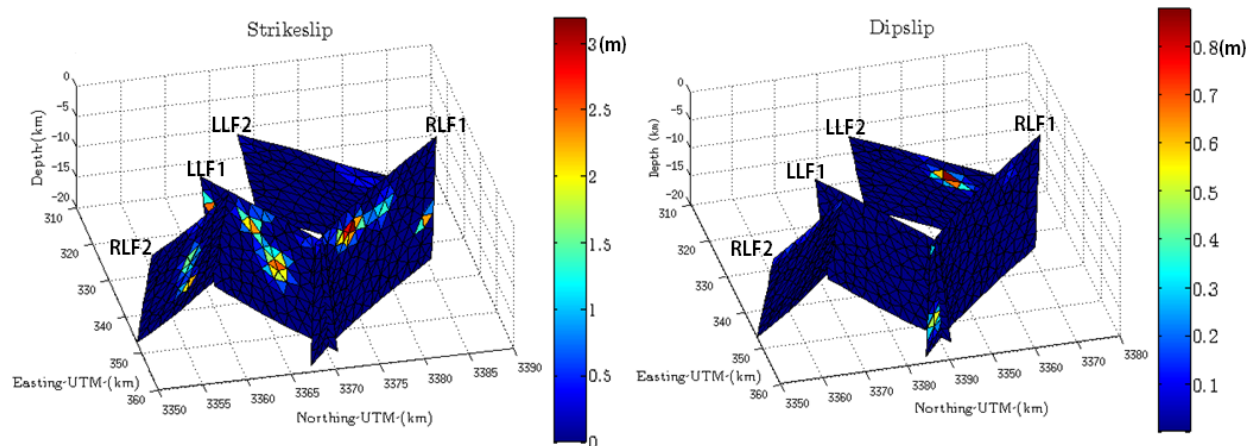


Figure 18. Slip distribution for the seismic sequence (the faults having straight strike). The top of the faults is 300 meters below the crust surface. The calculated magnitude (M_w) for RLF1, RLF2, LLF1 and LLF2 is 6.3, 6, 6.3 and 5.8 respectively.

5. References

- Abe T, Furuya M, Takada Y (2013)** Nonplanar fault source modeling of the 2008 M_w 6.9 Iwate–Miyagi inland earthquake in northeast Japan. *Bull Seismol Soc Am* 103, No. 1: 507–518
- Amarjargal S, Kato T, Furuya M (2013)** Surface deformations from moderate-sized earthquakes in Mongolia observed by InSAR, *Earth Planets Space*, 65, 713–723
- Bannert D, Bender F K, Bender H, Grüneberg F, Kazmi A H, Raza H A, Shams F A (1995)** *Geology of Pakistan*. Gebrüder borntraeger, Berlin
- Bernard M, Shen-Tu B, Holt I, Davis D M (2000)** Kinematics of active deformation in the sulaiman lobe and range, Pakistan. *J. Geophys. Res.* 105:13,253–13,279
- Furuya M, Kobayashi T, Takada Y, Murakami M (2010)** Fault source Modeling of the 2008 Inchan earthquake based on ALOS/PALSAR data. *Bull Seismol Soc Am* 100 (5B): 2750–2766. doi:10.1785/0120090242
- Fukuyama E (2015)** Dynamic faulting on a conjugate fault system detected by near-fault tilt measurements. *EPS*. doi:10.1186/s40623-015-0207-1
- Furuya M, Yasuda T (2011)** The 2008 Yutian normal faulting earthquake (M_w 7.1), NW Tibet: Non-planar fault modeling and implications for the Karakax fault. *Tectonophysics* 511:125–133. doi:10.1016/j.tecto.2011.09.003
- Geuzaine C, Remacle J F (2009)** Gmsh: A three-dimensional finite element mesh generator with built-in pre- and post-processing facilities. *Int J Numer Meth Eng* 79, no. 11: 1309–1331,
- Haq S S B, Davis D M (1997)** Oblique convergence and lobate mountain belts of Ister Pakistan. *Geology* 25:23–26
- International Seismological Centre (2012)** *On-line Bulletin*, <http://www.isc.ac.uk>, Internatl. Seis. Cent., Thatcham, United Kingdom. Accessed 01 Jan 2013
- Jarvis A, Reuter H I, Nelson A, Guevara E (2008)** Hole-filled seamless SRTM data V4, International Centre for Tropical Agriculture (CIAT). <http://srtm.csi.cgiar.org>. Accessed October 2012

- Jónsson S, Zebker H, Segall P, Amelung F (2002)** Fault slip distribution of the 1999 Mw 7.1 Hector Mine, California, earthquake, estimated from satellite radar and GPS measurements. *Bull Seismol Soc Am* 92 no. 4: 1377–1389
- Kazmi A H (1979)** Active faults systems in Pakistan. In: *Geol Surv Pak* (ed) *Geodynamic of Pakistan*. Quetta, Baluchistan
- Kazmi A H, Jan M Q (1997)** *Geology and Tectonics of Pakistan*. in: *Neotectonics*. pp:408,416. Graphic Publishers. Karachi. Pakistan
- Khan M A et al (2008)** Preliminary geodetic constraints on plate boundary deformation on the Ister edge of the Indian plate from TriGGnet (Tri-University GPS Geodesy Network). *J Him Geosci* 41: 71–87
- Kobayashi T, Takada Y, Furuya M, Murakami M (2009)** Locations and types of ruptures involved in the 2008 Sichuan earthquake inferred from SAR image matching. *Geophys Res Lett* 36 L07302. doi:10.1029/2008GL036907
- Lisa M, Jan M Q (2010)** Geoseismological study of the Ziarat (Balochistan) earthquake (doublet?) of 28 October 2008. *Curr. Sci.*, 98(1): 50–57
- Lohman R B, Simons M (2005)** Some thoughts on the use of InSAR data to constrain models of surface deformation: Noise structure and data downsampling. *Geochem Geophys Geosys*. doi: 10.1029/2004GC000841
- Maerten F, Resor P, Pollard D, Maerten L (2005)** Inverting for slip on three dimensional fault surfaces using angular dislocations. *Bull Seismol Soc Am* 95:1654–1665. doi:10.1785/0120030181
- Massonnet D, Rossi M, Carmona C, Adragna F, Peltzer G, Feigl K, Rabaute T (1993)** The displacement field of the Landers earthquake mapped by radar interferometry, *Nature*, 364, 138–142
- Meade B J (2007)** Algorithms for the calculation of exact displacements, strains, and stresses for triangular dislocation elements in a uniform elastic half space. *Comp and Geosci* 33: 1064–1075. doi:10.1016/j.cageo.2006.12.003
- Nakata T, Tsutsumi H, Khan S H, Lawrence R D (1991)** *Active Faults of Pakistan: Map Sheets and Inventories*. Research Center for Regional Geography, Hiroshima University, Hiroshima
- Okada Y (1992)** Internal deformation due to shear and tensile faults in a half-space. *Bull Seismol Soc Am* 82:1018–1040
- Pezzo G, Bancori J P M, Atroz S, Antonioli A, Salvi S (2014)** Deformation of the Ister Indian Plate boundary: insights from differential and multi-aperture InSAR data inversion for the 2008 Baluchistan (Ister Pakistan) seismic sequence. *Geophys. J. Int.* doi:10.1093/gji/ggu106
- Pinel-Puysségur B, Grandin R, Bollinger L, Baudry C (2014)** Multifaulting in a tectonic syntaxis revealed by InSAR: The case of the Ziarat earthquake sequence (Pakistan), *J. Geophys. Res. Solid Earth*, 119: 5838–5854. doi:10.1002/2013JB010564
- Rafi Z, Ahmad N, Rehman S U (2009)** Seismotectonic analysis of Ziarat, Balochistan earthquake of 29th October, 2008. Pakistan Meteorological Department. Technical report no. PMD-32/2009.
- Simons M, Fialko Y, Rivera L (2002)** Coseismic deformation from the 1999 Mw 7.1 Hector Mine, California, earthquake as inferred from InSAR and GPS observations. *Bull. Seismol. Soc. Am.* 92, no. 4: 1390–1402. doi: 10.1785/012000093
- Takada Y, Kobayashi T, Furuya M, Murakami M (2009)** Coseismic displacement due to the 2008 Iwate-Miyagi Nairiku earthquake detected by ALOS/PALSAR: preliminary results. *Earth Planets Space* 61:e9–e12

Tong X, SandIII D T, Fialko Y (2010) Coseismic slip model of the 2008 Inchan earthquake derived from joint inversion of interferometric synthetic aperture radar, GPS, and field data. *J. Geophys. Res.* Vol. 115:B04314. doi:10.1029/2009JB006625

Walker R T, Bergnan E A, Elliot J R, Fielding E J, Ghods A R, Ghorraishi M, Jackson J, Nazari H, Nemati M, Oveisi B, Talebian M, Walters R J (2013) The 2010–2011 South Rigan (Baluchestan) earthquake sequence and its implications for distributed deformation and earthquake hazard in southeast Iran. *Geophys. J. Int.* doi: 10.1093/gji/ggs109

Wright T J, Lu Z, Wicks C (2003) Source model of the Mw 6.7, 23 October 2002, Nenana Mountain earthquake (Alaska) from InSAR. *Geophys Res Lett.* doi:10.1029/2003GL018014

Yadav R B S, Gahalaut V K, Chopra S, Shan B (2012) Tectonic implications and seismicity triggering during the 2008 Baluchistan, Pakistan earthquake sequence. *J. Asian Earth Sci* 45: 167–178. doi: 10.1785/0120120133